Received: 24 December 2022 | Revised: 24 October 2023 | Accepted: 9 December 2023

DOI: 10.1002/mp.16934

RESEARCH ARTICLE

MEDICAL PHYSICS

Multibody dynamic modeling of the behavior of flexible instruments used in cervical cancer brachytherapy

Robin Straathof[1,2] | **Jaap P. Meijaard**[3] | **Sharline M. van Vliet-Pérez**[1,2] | **Inger-Karine K. Kolkman-Deurloo**[2] | **Remi A. Nout**[2] | **Ben J. M. Heijmen**[2] | **Linda S. G. L. Wauben**[1] | **Jenny Dankelman**[1] | **Nick J. van de Berg**[1,4]

[1]Department of BioMechanical Engineering, Delft University of Technology, Delft, the Netherlands

[2]Department of Radiotherapy, Erasmus MC Cancer Institute, University Medical Center Rotterdam, Rotterdam, the Netherlands

[3]Department of Precision and Microsystems Engineering, Delft University of Technology, Delft, the Netherlands

[4]Department of Gynecological Oncology, Erasmus MC Cancer Institute, University Medical Center Rotterdam, Rotterdam, the Netherlands

Correspondence
Robin Straathof, Department of BioMechanical Engineering, Delft University of Technology, Mekelweg 2, 2628 CD Delft, the Netherlands.
Email: r.straathof-1@tudelft.nl

Funding information
Dutch Research Council, Grant/Award Number: 17921; Dutch Cancer Society, Grant/Award Number: 17921; Top Sector Life Sciences & Health (LSH), Grant/Award Number: 17921

Abstract

Background: The steep radiation dose gradients in cervical cancer brachytherapy (BT) necessitate a thorough understanding of the behavior of afterloader source cables or needles in the curved channels of (patient-tailored) applicators.

Purpose: The purpose of this study is to develop and validate computer models to simulate: (1) BT source positions, and (2) insertion forces of needles in curved applicator channels. The methodology presented can be used to improve the knowledge of instrument behavior in current applicators and aid the development of novel (3D-printed) BT applicators.

Methods: For the computer models, BT instruments were discretized in finite elements. Simulations were performed in SPACAR by formulating nodal contact force and motion input models and specifying the instruments' kinematic and dynamic properties. To evaluate the source cable model, simulated source paths in ring applicators were compared with manufacturer-measured source paths. The impact of discrepancies on the dosimetry was estimated for standard plans. To validate needle models, simulated needle insertion forces in curved channels with varying curvature, torsion, and clearance, were compared with force measurements in dedicated 3D-printed templates.

Results: Comparison of simulated with manufacturer-measured source positions showed 0.5–1.2 mm median and <2.0 mm maximum differences, in all but one applicator geometry. The resulting maximum relative dose differences at the lateral surface and at 5 mm depth were 5.5% and 4.7%, respectively. Simulated insertion forces for BT needles in curved channels accurately resembled the forces experimentally obtained by including experimental uncertainties in the simulation.

Conclusion: The models developed can accurately predict source positions and insertion forces in BT applicators. Insights from these models can aid novel applicator design with improved motion and force transmission of BT instruments, and contribute to the estimation of overall treatment precision. The methodology presented can be extended to study other applicator geometries, flexible instruments, and afterloading systems.

KEYWORDS
cervical cancer brachytherapy, finite element modeling of source motion, flexible instrument, multibody dynamics

1 | INTRODUCTION

1.1 | Clinical motivation

Brachytherapy (BT) is an essential component in the curative treatment of cervical cancer.[1,2] In cervical cancer BT, a radioactive source that is mounted to a flexible cable is driven by an afterloader through channels in an intracavitary (IC) applicator and implanted interstitial (IS) catheters. The steep dose gradient in BT, with a typical dose fall-off of 5–12% per mm at 1–3 cm of the source axis, enables local delivery of a high dose to the target region with limited dose in surrounding organs-at-risk (OARs) and healthy tissue.[3] However, this makes the delivered dose and the outcome of BT particularly susceptible to geometric variations in source positioning. The impact of geometric variations associated with the accuracy of applicator reconstruction and (afterloader) source positioning in IC applicators on target and OAR dose-volume histogram (DVH) parameters has been estimated to be 4% (SD, $k = 1$) of the dose per fraction.[4] Geometric source positioning variations should be minimized as these may systematically affect the dose delivered per fraction, impacting predicted local control and morbidity.[5] Related is the ability to accurately position IS needles in the presence of tissue and applicator forces.[6,7] The behavior of flexible BT instruments, such as afterloader source cables or needles, in applicators therefore needs to be well understood, whereas the focus in literature has been on quantifying position variations. This knowledge may additionally aid automated planning of curved source and needle channels in patient-tailored BT applicators, for which constraints on curvature, clearance, and torsion need to be set to ensure that instruments can be predictably inserted.[8–11]

1.2 | Related work

Sent by the afterloader, the source traverses through the lumen of transfer tubes, the applicator, or catheters. Source cable behavior is predominantly characterized by two effects: “curving” and “snaking”. As the diameters of the inner lumen of applicators, transfer tubes and catheters are larger than the source diameter, the source trajectory can deviate from the (curved) centerline; referred to as “curving” (Figure 1a).[12] Kohr and Siebert clearly illustrated the resulting offset from the channel centerline of a flexible implant tube as a function of the radius of curvature.[13] Furthermore, “snaking” occurs when the source cable curls in the lumen as the result of friction or obstruction along the channel (Figure 1b).[12] Snaking also results in axial source path deviations. In multiple studies, geometric variations associated with these effects have been quantified. Humer et al. found mean deviations in ring applicators of 3.2–4.5 mm between dwell positions determined using video analysis and planned positions on the centerline, depending on the diameter of the ring.[14] The use of manufacturer-measured source positions, or those obtained from applicator commissioning,[3] is therefore recommended in treatment planning systems (TPS). Nevertheless, maximum deviations up to 2.6 mm along the source path in ring applicators were noted between manufacturer-supplied paths and those measured with gafchromic film.[15] In addition, mean absolute differences up to 1.8 mm for the source position and 21.8° for the source orientation were found between the manufacturer’s data and localized using three-dimensional imaging in a ring applicator.[16] Source positions were observed on CT to differ up to 2.5 mm from the path provided by vendor marker wires.[17] These results suggest that maximum source positioning deviations may be of several millimeters in clinical practice, and may exceed common accuracy guidelines of 2 mm.[18,19]

Flexible catheters or needles may be embedded in templates, guided by curved channels (e.g., in vaginal caps) of hybrid IC/IS applicators, or passively steered in patient-tailored applicators.[8,9,20–22] Needle insertion force and tip placement accuracy in a rigid channel are predominantly affected by the bending stiffness of the needle, radius of curvature of the path, and friction parameters. Reproducibility of tip positions of flexible needles inserted in channels of varying curvature was shown to be high <1 mm.[23] Furthermore, it has been shown that peak insertion forces of needles in single curved channels are strongly related to the channel’s radius of curvature.[8] However, an accurate understanding of what influences flexible instrument behavior in the curved channels of hybrid intracavitary-interstitial (IC/IS) applicators is still lacking.

As of yet, no dynamic models have been introduced for simulating the behavior of flexible instruments in BT. Kinematic models for BT catheters in curved channels that have been introduced were based on models for steerable needles.[9–11] The modeling of deformations and associated forces and moments of slender elastic rods inside rigid (circular) channels or environment has been the topic of several studies for different applications: (i) drill string buckling,[24–27] (ii) serpentine locomotion,[28–30] (iii) concentric tube instruments,[31–33] and (iv) (steerable) catheter and guidewire insertion,[34–44] among others. Due to geometric, material, and physical nonlinearities in the problem formulation, most work resorts to numerical approaches. Of particular interest are flexible multibody link methods which can achieve a high accuracy but generally are computationally intensive, and rigid multibody link methods which are more tractable but require a larger number of segments to achieve similar accuracy.[34]

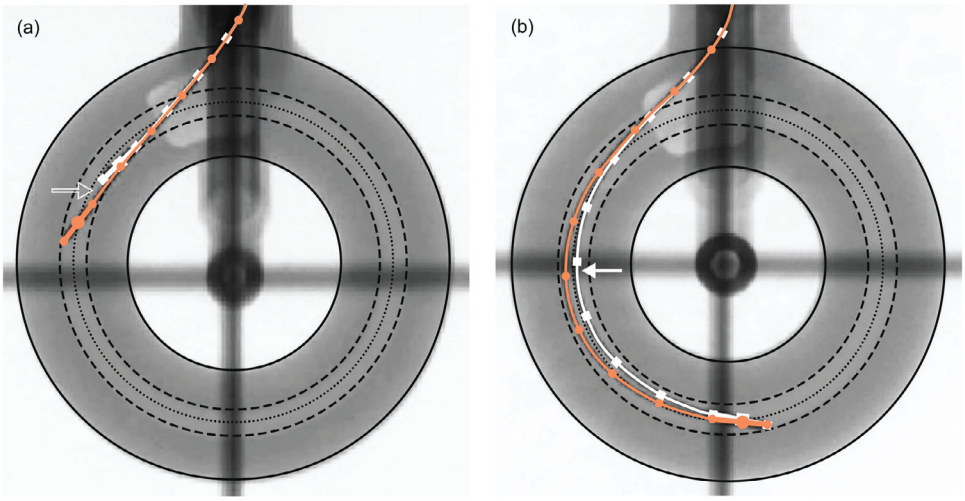

FIGURE 1 Schematic illustration of the source cable configuration at several dwell positions inside a Ø34 mm Ring CT/MR applicator (Elekta Brachytherapy, Veenendaal, the Netherlands). Two source cable states in succession are indicated by the white solid line with square markers and the orange solid line with round markers respectively. (a) During ring entry, the source travels almost in a straight line (marked by the hollow arrow). (b) Mid-applicator the source center remains almost stationary between successive dwell positions due to friction, whereas the source cable snakes towards the outer wall of the applicator (marked by solid arrow). Figures adapted from the Oncentra® Brachy v4.6 manual.[56]

1.3 | Contribution

The purpose of this study is to develop and validate computer models to simulate: (1) BT source paths, and (2) insertion forces of needles in curved applicator channels. Flexible instruments are modeled and simulated in SPACAR, which is a program that allows for finite element analysis of multibody dynamic systems with flexible or rigid links.[45] Simulations using this program have shown excellent agreement with experimental results for constrained elastic rods.[37,46] The main benefits of such an approach are that this improves understanding of instrument behavior and enables systematic testing of the influence of design parameter changes on the behavior of instruments used in BT. As such, applicator channels can be designed that guide sources or needles more effectively, while reducing the need for continuous experimental validation and potentially individual applicator commissioning.

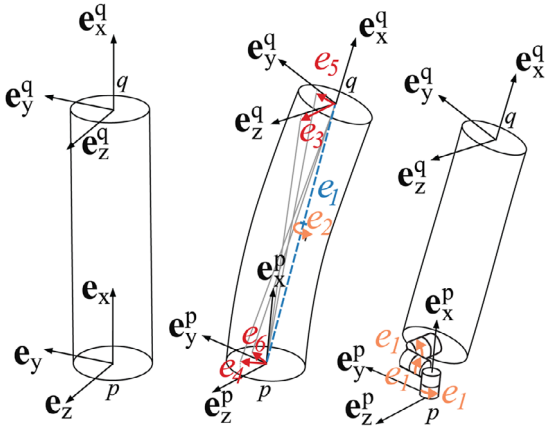

FIGURE 2 Reference beam configuration (left) and two representations of deformed beam configurations (middle and right). The beam configuration in the middle shows six deformation modes for a flexible beam element: elongation (e_1), torsion (e_2), and bending (e_{3-6}). The beam configuration on the right is similar to the configuration in the middle, but this is achieved through three relative rotations (e_1) of connected hinges drawn as cans in series, whereas the beam itself is rigid. Figure adapted from Jonker and Meijaard.[63]

2 | MATERIALS AND METHODS

2.1 | Finite element model of elastic rods

In this study, we model flexible instruments propagating through and interacting with curved channels as flexible or rigid multibody link systems in three-dimensional space. Simulations are performed using SPACAR 2017,[45] implemented in MATLAB R2021b (Mathworks, Natick, MA, USA). For an extensive description of SPACAR the reader is referred to the dissertation by Jonker.[47]

For the flexible multibody model, the instrument is modeled as a set of flexible (planar) beam elements. For flexible beam elements, deformations in all directions with the exception of elongation are permitted (Figure 2). The bending stiffness, $S_{\text{flex},3..6} = EI$, of these elements is obtained from experiments. Torsional stiffness, $S_{\text{flex},2} = GJ$, is estimated assuming isotropic material behavior. In the case of rigid multibody analysis, the instrument is modeled as a set of rigid multibody links interconnected with hinge elements (Figure 2). For rigid multilink simulation, the bending stiffness of a joint is found by equaling

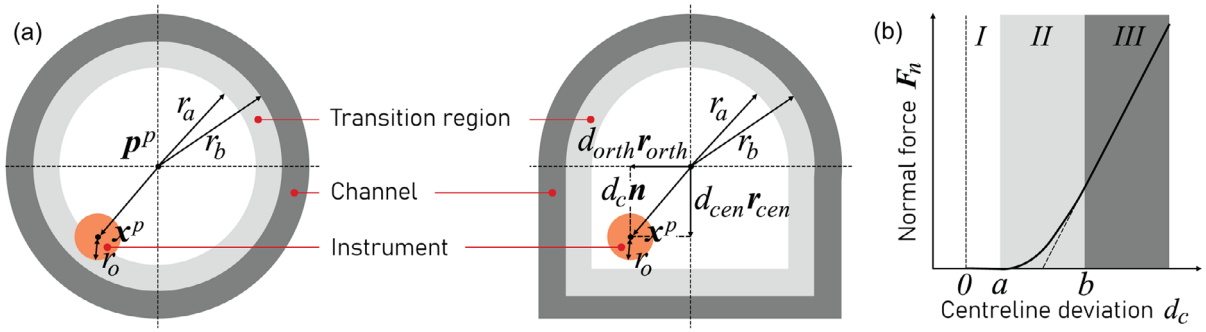

FIGURE 3 (a) Contact detection model for circular and U-shaped channels. (b) Normal force model in a circular channel. Figure adapted from Khatait et al.[46]

the strain energy resulting from bending with the energy stored by a torsion spring[48]:

$$U = \frac{1}{2} S_{\text{rig},1} \theta^2 = \frac{EIl}{2R^2} \tag{1}$$

Here, θ is the angle subtending the element, R the bending radius, and l the element length. Observing that $\theta = l/R$, the stiffness of the joint in bending is:

$$S_{\text{rig},1} = \frac{EI}{l} \tag{2}$$

The stiffness of the torsion springs in the axial direction of the instrument is found via $S_{\text{rig},1} = \frac{GJ}{l}$.

2.2 | Contact detection and friction model

To guide the flexible instrument through the channel, loads are applied on the nodes of the multibody model. In the case of both a lumen and instrument with a circular cross-section, contact may be defined to occur when the instrument's centerline deviation is greater than the difference in radius of both elements (Figure 3). For each node of the instrument, $\boldsymbol{x}^p$, the Euclidean distance to the centerline is computed using the MATLAB function distance2curve.[49] This function returns the distance to the centerline, d_c, and the closest point on the centerline $\boldsymbol{p}^p$. The normal and tangent vectors are computed respectively as follows:

$$\boldsymbol{n} = \frac{\boldsymbol{x}^p - \boldsymbol{p}^p}{||\boldsymbol{x}^p - \boldsymbol{p}^p||}, \quad \boldsymbol{t} = \frac{\dot{\boldsymbol{x}}^p - v_{c,n}\boldsymbol{n}}{\left|\left|\dot{\boldsymbol{x}}^p - v_{c,n}\boldsymbol{n}\right|\right|} \tag{3}$$

The velocities $v_{c,t}$ and $v_{c,n}$ are the tangential and normal components respectively of the instantaneous velocity $\boldsymbol{v}_c$ at the point of contact. This is computed from the nodal translation velocity $\dot{\boldsymbol{x}}^p$ and angular velocity $\boldsymbol{\omega}^p$:

$$\boldsymbol{v}_c = \dot{\boldsymbol{x}}^p + r_o \boldsymbol{\omega}^p \times \boldsymbol{n} \tag{4}$$

Where, $(0, \boldsymbol{\omega}^p)^{\mathsf{T}} = 2\bar{\boldsymbol{Q}}^{p\mathsf{T}} \dot{\boldsymbol{\lambda}}^p$, and $\bar{\boldsymbol{Q}}^p$ is a quaternion matrix.[50] To aid the convergence of SPACAR, the contact model by Khatait et al. is used to determine the normal force $\boldsymbol{F}_n$ acting on the point of contact, which distinguishes three different regions (see Figure 3).[36] To compute the tangential force $\boldsymbol{F}_t$ at this point, the friction model used by Khatait et al. is adapted in this work to also include the Stribeck friction effect (without viscous friction).[51] Taking into account the instrument's radius, r_o, this results in the following equivalent loads on a node:

$$\begin{cases} \boldsymbol{F} = \boldsymbol{F}_t + \boldsymbol{F}_n \\ \boldsymbol{M} = r_o\, \boldsymbol{n} \times \boldsymbol{F}_t \end{cases} \tag{5}$$

The extension of this model to channels with convex polygonal cross-sections is feasible with a series of if-statements (Figure 3).

2.3 | Simulation

Two types of instrument interactions relevant for cervical cancer BT were modeled:

1. BT source positioning in the rings of ring applicators;
2. Needle insertion in S-shaped channels.

Interaction forces and input motions are specified with user-defined functions. At the proximal end of the instrument, an input motion is applied and rotations and displacements in non-axial directions are fixed. For integrating the equations of motion, the default Shampine-Gordon variable-order, variable-stepsize integrator is used with error tolerances of $1 \cdot 10^{-7}$ or $1 \cdot 10^{-4}$, for source path and insertion force simulations, respectively.[52]

To aid the convergence of simulations, several parameters were manually tweaked. The total number of segments used for modeling the instrument contributes to both the accuracy and the computation time. The number of elements was increased until convergence, that is, accuracy of the solution would no longer visibly

TABLE 1 List of parameters used in SPACAR analysis of BT source positioning in an applicator channel and insertion of combined catheter and obturator in a 3D-printed template.

Sym.	Description, unit	BT source positioning				Needle insertion
μ_k	Kinetic friction coefficient	0.20				0.074
μ_s	Static friction coefficient	0.25				0.094
c_w	Wall damping, Ns/m	10				10
EI	Flexural rigidity, Nm^2	$5.2 \cdot 10^{-5}$	(thin)	$1.8 \cdot 10^{-4}$	(thick)	$1.2 \cdot 10^{-2}$
GJ	Torsional rigidity, Nm^2	$4.0 \cdot 10^{-5}$	(thin)	$1.4 \cdot 10^{-4}$	(thick)	$9.6 \cdot 10^{-3}$
k	Wall stiffness, N/m	$1 \cdot 10^5$				$1 \cdot 10^6$
l_{rig}	Length per element rigid, mm	3	(thin)	10	(thick)	3.3
l_{flex}	Length per element flexible, mm	5	(thin)	10	(thick)	5
$\mathcal{L}$	Length of instrument, m	0.105	(thin)	0.616	(thick)	0.12
m/l	Mass per unit length, kg/m	0.04	(rigid)	0.1	(flex.)	1
r_a	Radius transition zone, mm	1.4				1.2 – 1.4 (tol. +0.1)
r_b	Radius channel, mm	1.5				1.3 – 1.5 (tol. +0.1)
r_o	Radius instrument, mm	0.25	(thin)	0.425	(thick)	0.99
v_{brk}	Breakaway velocity, m/s	0.001				0.001
v_{in}	Input velocity, m/s	0.5				0.1

improve. The mass per unit length of the elements was increased to reduce the eigenfrequency of the elements which enables larger time steps, while maintaining stable simulations and thereby increasing convergence.[53] Similarly, the insertion velocity could be increased to increase computation speed. To ensure that inertia forces remained small, upper limits were specified for both parameters. Contact parameters were varied to increase the size of the transition regions of the normal force and Stribeck friction models. Model parameter values are listed in Table 1. Computational speed improvements of roughly a factor 10−20 were achieved through these changes. All simulations were performed on a machine with an Intel i7 1.8 GHz CPU.

The MATLAB-code for the simulation of flexible instruments in channels using SPACAR along with supporting documentation is made freely available in a repository to support independent research.[54] Researchers are encouraged to reproduce results in this work, as well as to extend the use of the models.

2.4 | Experimental setup and conditions

For evaluating the source cable model, paths of a Flexitron® source cable (Elekta Brachytherapy, Veenendaal, the Netherlands) were simulated in the rings of Ring CT/MR applicators (Elekta, diameter: 26, 30, and 34 mm, angle: 45° and 60°). Simulated dwell positions were validated against the coordinates measured by the applicator manufacturer. A comparison was also made when considering dwell positions to be spaced along the channel centerline. Centerline, manufacturer-measured source path and other applicator data (e.g., lumen diameter) were exported from Oncentra® Brachy V4.5 (Elekta) to MATLAB. The centerline data were adjusted based on CT measurements and digital images of specific applicators to correct for known deviations between the actual and digitized centerline at the proximal part of the ring, and used to construct the channel for SPACAR analysis. As a simplification and to aid convergence, a constant speed insertion was modeled toward the MR line marker, which corresponds with the most distal dwell position. Manufacturer-measured dwell positions imported were spaced 1 mm apart. Differences between manufacturer-measured dwell positions and the simulated dwell positions or those spaced on the centerline were calculated using Euclidean distances. Angular deviations were determined between manufacturer-specified source orientations, which are approximated as the tangent of the centerline, and the simulated source orientations.

In order to assess the impact of differences in source positions on dosimetry, standard plans were generated for all six applicator geometries based on manufacturer-measured dwell positions spaced 5 mm apart with a prescribed 100% dose to Point A. The resulting dwell times were transferred to corresponding simulated and centerline positions. Relative dose differences between the standard plans and plans for simulated and centerline positions were evaluated at Point A to approximate the effect on the target volume. In addition two points were selected on the lateral surface of the rings and two points lateral from the surface at 5 mm depth, that serve as vaginal dose points, as the largest dosimetric effects were expected in the ring plane.[55]

For evaluating the needle insertion models, simulated ProGuide 6F catheter with obturator (Elekta)

insertion forces in S-shaped channels were compared with experimental force measurements in dedicated 3D-printed templates. These applicator templates were developed in SolidWorks 2021 software (Dassault Systèmes, Vélizy-Villacoublay, France), and converted to STL. The templates were 3D-printed by Oceanz (Ede, the Netherlands) using selective laser sintering (SLS) on an EOS Formiga P1 system (EOS, Krailling, Germany) using PA-12 (EOS PA 2200, Krailling, Germany). All templates were printed in the same orientation, such that the proximal end of channels aligned with the vertical axis. The templates contained a set of S-shaped channels with the following characteristics based on earlier experiments[8]:

1. Radius of curvature r ranging from 20 to 60 mm in 5 mm increments with zero torsion and a channel diameter of 2.6 mm;
2. Torsion τ, that is, a measure of planarity of the curve, in the middle straight section ranging from 0 to π in five steps with radius of curvature 35 mm and a channel diameter of 2.6 mm;
3. Channel diameter $\varnothing$ ranging from 2.6 to 3.0 mm in three steps with zero torsion and a radius of curvature of 35 mm.

To correct for known shrinkage in the 3D-printing process, a tolerance of +0.2 mm on the channel diameter was used in the computer designs. Channels were post-processed to ensure that the diameters were within this range. To account for this experimental uncertainty in the channels' diameter, all insertion force simulations in SPACAR were performed using both the nominal and increased diameter. The experimental setup is shown in Figure 4. The template was bolted to two perpendicularly mounted translation stages (PT1/M, Thorlabs, Newton, New Jersey, USA) which enabled accurate positioning of the template. The obturator was fully inserted into the catheter and held by a 3D-printed clamp, such that the free catheter length was 120 mm. This clamp was mounted to a one degree-of-freedom (DOF) load decoupler which housed a load cell (Futek LSB200, Irvine, USA). The sampling frequency was 5000 Hz. Displacements at a fixed translation velocity of 5 mm/s were imposed by a linear stage (Aerotech PRO 115, Pittsburgh, USA) using a controller board (DS1104, dSPACE, Paderborn, Germany) running on a dedicated PC with in-house developed interface. All insertion conditions were repeated five times. Force data were processed in MATLAB with a central moving average filter with a kernel size of 241. The influence of 3D-printing manufacturing tolerances -and in particular in the channel diameter- on force measurements was estimated. Inter-template (same channel designs in different templates) and inter-channel variations (same channel designs in same template) in force measurements were quantified and normalized based on the peak insertion force at the

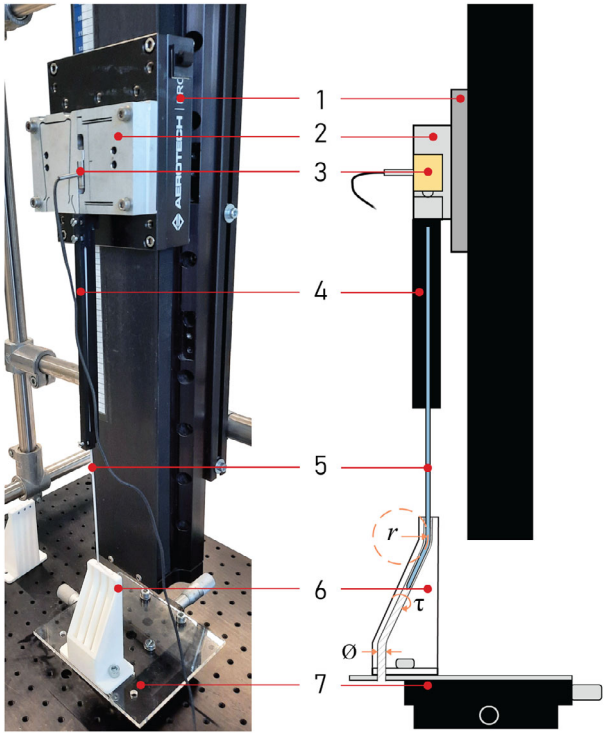

FIGURE 4 Photograph and schematic illustration of setup for measuring the insertion force in templates with S-shaped channels, with channel design parameters radius of curvature r, torsion τ and diameter $\varnothing$ indicated. Shown are: (1) linear stage, (2) axial force decoupler, (3) load cell, (4) connecting piece, (5) catheter and obturator, (6) template, and (7) translation stages.

first bend of channels with radius of curvature 35 mm and a nominal lumen diameter of 2.6 mm. Expanded inter-template and inter-channel insertion force uncertainties ($k = 2$), including measurement uncertainty, for these templates were 11.9% and 8.2%, respectively.

Mechanical properties of the BT source cable and combined catheter and obturator were unknown. For these tests a check cable, which is identical to the Flexitron source cable, was used. The bending rigidity was estimated using a standard three-point bending test. The machine used for load testing was the linear uni-axial testing machine Zwick Z005 (Zwick/Roell, Venlo, the Netherlands). A displacement was imposed and the resulting reaction force was measured using a load cell (KAF-TC 1 kN, Zwick/Roell). Bending rigidity of the source cable was determined at both the thin (adjacent to the source) and thick (remaining part of the cable) sections. The friction coefficients between the source cable and the applicator were estimated. Friction coefficients between the catheter and templates were determined experimentally. Two parts were 3D-printed to clamp the needle with a controllable constant normal force through a compression spring. During needle motion, the axial force was measured on a linear stage using a 1-DOF load cell. The static friction coefficient was determined at the maximum global peak axial force,

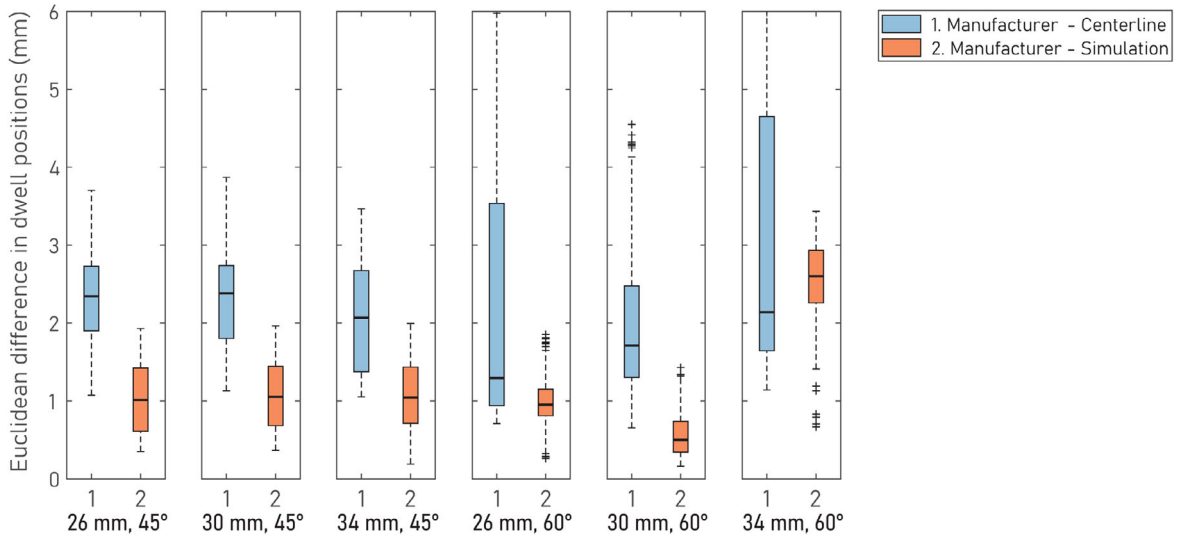

FIGURE 5 Boxplot showing Euclidean (3D) distances between the manufacturer-measured source positions and the centerline or simulated dwell positions for varying applicator geometries. The black line indicates the median, the boxes the interquartile ranges, the whiskers the extrema without outliers, and the crosses the outliers.

and the kinetic friction coefficient as the mean of the axial force measurements during the kinetic phase. In Table 1 the resulting parameter values used for SPACAR simulation are shown.

3 | RESULTS

3.1 | Source positioning

The results treated in this section concern those obtained using rigid multibody models as these outperformed flexible multibody models in terms of computation time (20–30 min vs. >6 h) and convergence (guaranteed vs. not guaranteed). Euclidean distances between the manufacturer-measured source positions and the centerline or simulated dwell positions are illustrated in Figure 5. Median and maximum differences between dwell positions along the centerline and the positions measured by the manufacturer are 1.3–2.4 mm and 3.5–6.3 mm respectively across applicators of different geometries. Simulated dwell positions are in closer agreement with manufacturer-measured dwell positions than centerline dwell positions, with median and maximum differences of 0.5–2.6 mm and 1.4–3.4 mm respectively for applicators of varying geometries. As can be observed in the figure, agreement between the simulated and manufacturer-measured dwell positions is the lowest for the ∅34 mm/60° applicator. Except for this applicator, maximum deviations between the simulations and manufacturer-measured data are <2.0 mm. Maximum angular deviations between manufacturer-specified source orientations and simulated source angles amount to 26.0°–32.7°. These deviations are the largest in the distal part of the applicator.

Figure 6 shows the simulated and manufacturer-measured source trajectories in two exemplary applicator sets: the ∅26 mm/60° and ∅34 mm/60° applicator. The source path determined using rigid multibody model simulation closely resembles the manufacturer-measured source path in the former applicator (Figure 6a, Video in Supplementary Material). At the proximal part of this ring applicator, the simulation and measurements by the manufacturer indicate a straight-line motion after exiting the plastic tube insert. The source is then pushed against the flat section of the U-shaped channel where it attains a maximum deviation orthogonal to the centerline of approximately 1.1 mm (the theoretical maximum is 1.5 mm). Halfway through the ring the simulation indicates source stalling. Figure 7 shows the forces on the source cable during source stall, where friction is shown to cause rotation of the source as well as cable snaking. Increased contact of the cable with the applicator channel wall causes the inter-dwell distance to slightly decrease compared to the nominal step size. The difference between the central and manufacturer-measured or simulated trajectory is therefore the largest at the most distal dwell position. Dwell positions obtained through simulation in the ∅34 mm/60° applicator have the worst conformance to the manufacturer-measured source path (Figure 6b). As can be observed in this figure, this is primarily the result of a persisting offset along the source path that is already visible at the proximal part of the ring. Moreover, differences between simulated and manufacturer-measured paths arise in the stalling phase, halfway through the ring.

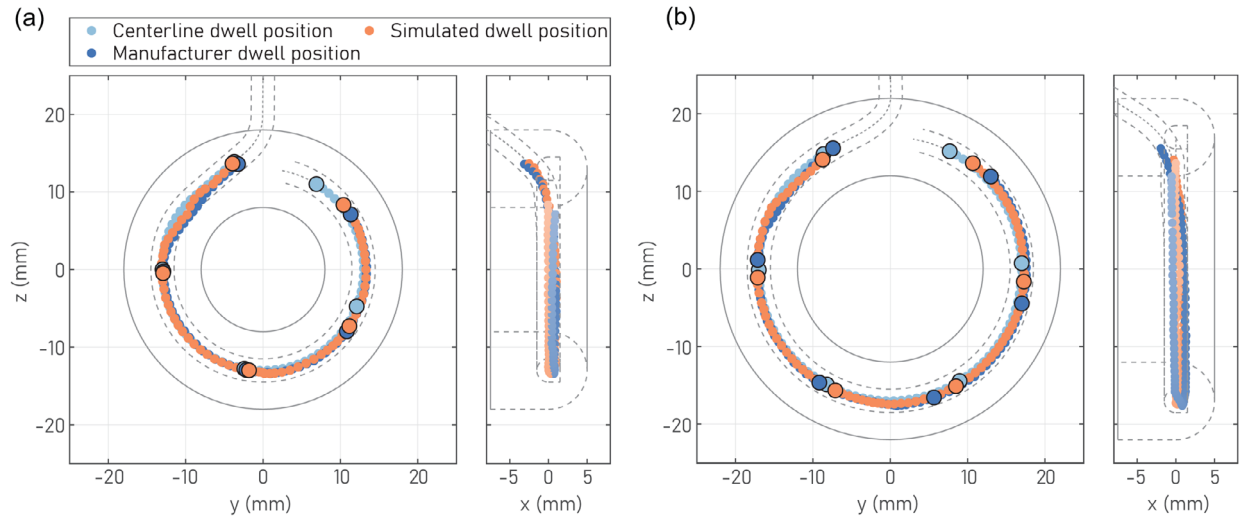

FIGURE 6 Simulated and manufacturer-measured dwell positions in two exemplary applicator sets, (a) the ∅26 mm/60° and (b) ∅34 mm/60° applicator. Views of the dwell positions projected onto the ring plane and orthogonal to this plane are shown.

TABLE 2 Relative absolute dose differences between standard plans based on manufacturer-measured dwell positions and plans for simulated or centerline dwell positions. Differences for all applicator geometries are expressed in median (range).

	Point A dose difference (%)	Lateral surface dose difference (%)	Lateral 5 mm dose difference (%)
Standard—centerline plan	0.9 (0.3 – 1.9)	6.2 (0.6 – 12.0)	3.0 (0.1 – 7.1)
Standard—simulated plan	0.4 (0.0 – 1.3)	1.1 (0.8 – 5.5)	2.8 (1.6 – 4.7)

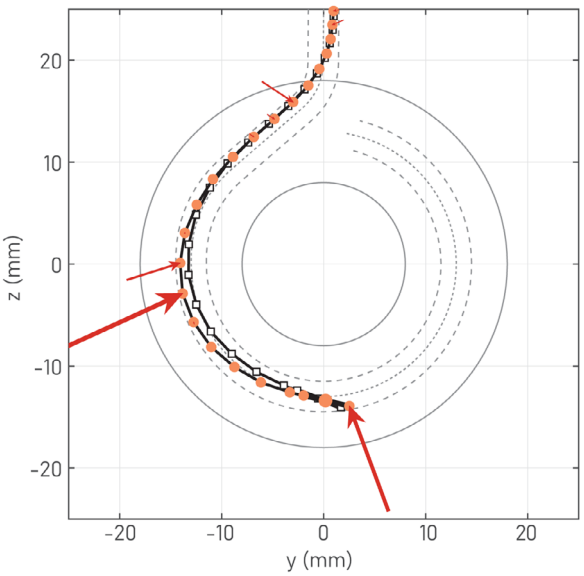

FIGURE 7 Simulation of the force vectors (red arrows) acting on the nodes of the source cable at the point of source stalling and cable snaking in a ∅26 mm/60° applicator. Two source cable states in succession are indicated by the solid line with white square markers and the solid line with orange round markers, respectively.

Dose differences between standard plans based on manufacturer-measured dwell positions and applied to simulated or centerline dwell positions are shown in Table 2. Discrepancies between centerline and manufacturer-measured dwell positions resulted in absolute relative dose differences of a maximum 1.9%, 12.0%, and 7.1% for Point A, the lateral surface of the ring and at 5 mm depth, respectively. Maximum relative dose differences are smaller between simulated and manufacturer-measured dwell positions and amount to 1.3%, 5.5%, and 4.7%, respectively.

3.2 | Needle insertion force

As discretization errors were apparent in flexible multilink models, the results treated in this section again concern those obtained using rigid multibody models. The computing times of these rigid multibody models were around 15–25 min, versus 2–6 h for the flexible models. Needle insertion simulations and experimental measurements were performed in S-shaped channels of varying curvature, torsion, and diameter. Figure 8 illustrates the simulated and experimental (median) axial insertion force versus insertion depth profiles for needle insertion in channels with varying radius of curvature. As can be observed from this figure, the simulation results accurately resemble the experimentally measured force-depth profiles. The force-depth profiles show

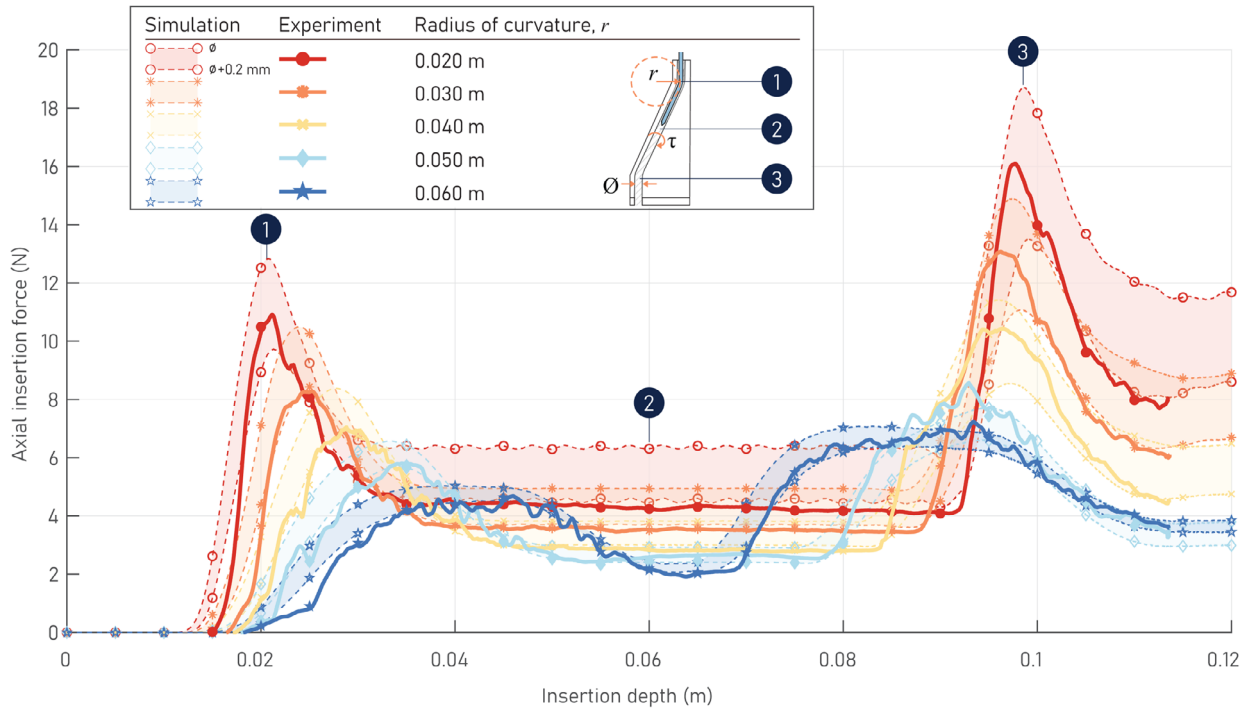

FIGURE 8 Simulated and experimental (median) axial insertion force versus insertion depth profiles of a ProGuide 6F catheter and obturator in planar S-shaped channels with varying radius of curvature (0.020 m–0.060 m). Shaded regions indicate the range between simulated solutions generated for nominal (2.6 mm) and increased channel diameters (2.8 mm). The numbers (1)–(3) indicate the 1st peak, plateau region, and 2nd peak, respectively.

two distinct force maxima, which occur at both curves of the S-shaped channel, and a plateau region in between. Peak forces in successive curves seem to be additive, that is, the peak forces generated in the second curve are the same as that in the first curve. The simulated and experimental peak and plateau insertion forces in channels with different design parameters are shown in Figure 9. For all tested channel design parameters, the experimental results are in good agreement with the predicted peak and plateau forces, that is, within the range of simulated results yielded by including experimental uncertainty. The plot shows that with increasing radius of curvature, peak and plateau insertion forces asymptotically decrease. For the developed templates, cumulative torsion is of small impact on the magnitude of peak and plateau forces. However, additional tests showed that torsion may affect the insertion force depending largely on the coefficient of friction and the distance between the curves (data not shown). Last, with increasing channel diameter, that is, larger clearance between instrument and channel, peak and plateau forces decrease.

4 | DISCUSSION

The purpose of this study was to develop and evaluate multibody dynamic models that can be used for the simulation of source cables and needles in curved applicator channels. Rigid and flexible multibody model kinematics and dynamics were formulated. Simulations were performed in SPACAR, for which contact forces and motion inputs were defined in MATLAB. Parameter inputs for the simulations were calculated, experimentally obtained, or chosen to aid convergence. The models developed show promising results in simulating the behavior of source cables and needles in brachytherapy applicators. Simulated dwell positions were generally in acceptable agreement with the dwell positions measured by the manufacturer. Simulated needle insertion force-depth profiles and peak and plateau insertion forces in curved channels of varying geometries resembled those obtained by the experiment.

In this work, both rigid and flexible multibody models were developed. Both methods have shown to be suitable for the simulation of elastic rods in channels in literature.[34] However, as the small radii of curvature of the channels studied in this work necessitate the use of many nodal contact points, rigid multibody models outperformed the flexible models in terms of computational speed, convergence and accuracy (due to discretization errors).

Due to the small radius of curvature and the relatively large lumen diameter of ring applicators, actual dwell positions may substantially deviate from nominal ones on the centerline. Therefore, it is better to use the source path measured by the vendor of the applicator

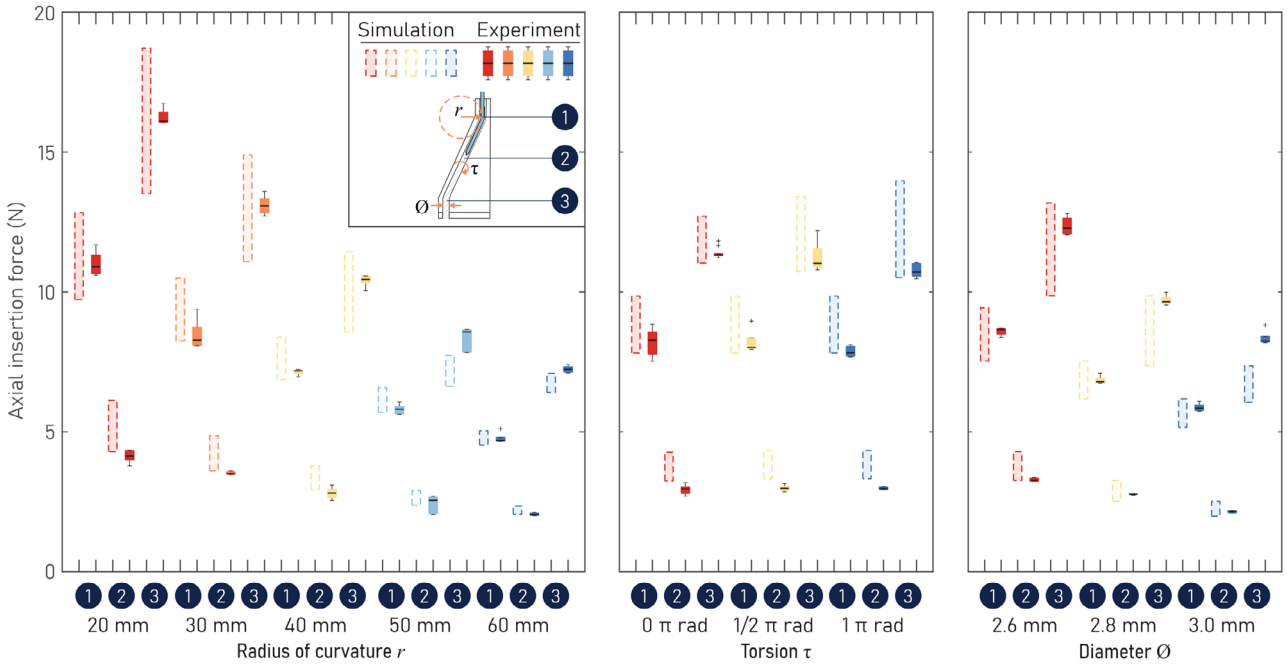

FIGURE 9 Boxplot showing simulated and experimental peak and plateau axial insertion forces of a ProGuide 6F catheter and obturator in S-shaped channels with varying design parameters radius of curvature r, torsion τ and diameter $\varnothing$. Shaded regions with dotted outlines indicate the range between simulated solutions generated for nominal and increased channel diameters (+0.2 mm). For the experimental measurements, the black line indicates the median, the boxes the interquartile ranges, the whiskers the extrema without outliers, and the crosses the outliers.

in the TPS. Simulations of the Flexitron® source cable in Ring CT/MR applicators in this study in general showed acceptable agreement with manufacturer-measured source paths, with median and maximum differences of 0.5–1.2 mm and <2.0 mm respectively for all applicator geometries except the ⌀34 mm/60° applicator. These findings are similar to those presented by Goulet et al.,[16] and within commonly specified accuracy guidelines.[18,19] The impact on dosimetry was found to be moderate, with maximum relative differences of 5.5% and 4.7% in points at the lateral surface and at 5 mm depth of the ring. Several factors may explain the deviations between simulated and manufacturer-measured source data in this work. Estimation of model parameters, and in particular friction coefficients, may have affected the accuracy of the simulation.[37,46] In addition, several modeling simplifications were made, including the use of a simplified contact model, omission of transfer tubes, and constant speed insertions. Stepwise input motion patterns can be implemented, but differences in positioning between stepwise and full runs are likely small,[56] and this may require model damping to not detriment (speed of) convergence,[57] or the use of a more stable (implicit) integration scheme. Finally, the actual centerline may deviate from the digitized centerline. Some articles suggested that applicator geometries may not always be consistent,[15] but the vendor's source paths are based on averaged coordinates over several samples, and in general the related uncertainty - including measurement uncertainty- is noted to be small (sub-millimeter).[56,58]

Several studies and guidelines have advocated for individual applicator commissioning,[3,12,15,16] based on measurements with maximum deviations of several millimeters with manufacturer-measured source paths. For this purpose several types of applicator commissioning methodologies have been proposed in literature. Results from simulations in this work emphasize that 3D commissioning methods are preferred over 2D methods, such as autoradiography or video analysis, due to deviations of approximately 1 mm orthogonal to the centerline. This is supported by other work.[16,56] It is not clear what causes the differences between vendors' measured source paths and those measured by institutes. This may have to do with variations in previously used commissioning methodologies, such as transfer tube curvature and applicator alignment,[59,60] and the use of source cable surrogates,[17] or uncertainties associated with source cable/applicator/afterloader combinations.[15,56,58] One of the benefits of the models in this work is that these can facilitate systematic testing of the influence of input parameters such as centerline geometries, flexible instrument properties, and afterloading systems, as well as the effects of noise and disturbances in these parameters.

The obtained insertion force-depth characteristics of flexible instruments in S-shaped channels was similar to those found by Liu et al., who developed models of

flexible instruments (catheters) in planar curved channels with clearance and friction based on the definition of contact patterns.[44] Our work differs from the article by Liu et al. in that it considers application of external loads on the nodes, rather than making use of contact patterns. Although computationally more intensive, the models in this work enable easy implementation of 3D reference curves and complex channel cross-sections. Insertion force-depth profiles of the catheter and obturator in S-shaped channels were shown to be strongly affected in this work by the curvature and diameter - and to a lesser extent torsion- of these channels. It has been theoretically shown that the insertion force increases exponentially with cumulative curvature for a rod with negligible bending rigidity,[43] or quadratically in a frictionless and zero-clearance channel.[30] Laan et al. similarly showed that the insertion forces of catheters and obturators increase in channels with decreasing radius of curvature.[8] Differences between the measured peak insertion forces in this work and the latter may be explained by the difference in coefficient of friction between instrument and channel, which (theoretically) may be exponentially related to the required insertion force.[37,43,46] The effect of channel diameter on the insertion force of elastic rods in curved channels has been scarcely studied, although the work by Liu et al. provides some insights.[44] The strong dependence of flexible instrument behavior on channel diameter stresses the importance of adequate applicator (channel) geometry consistency checks, especially when considering 3D printing.

The methodology introduced in this work has several limitations. First, this work aimed to develop and validate source cable simulations, of which the latter was based on comparing geometric differences between simulated and manufacturer-measured or centerline dwell positions. The impact of these geometric differences was investigated on dose points defined relative to the applicator and not on dose-volume histogram parameters or ICRU points. In addition, a standard plan was used with constant dwell times, whereas clinical dwell times are more heterogeneous due to dwell time optimization and therefore more prone to variations. Nevertheless, previous studies have indicated that the dosimetric impact of source position variations may be limited on clinically relevant dose points or volumes, and especially that of the clinical target volume, with possible exceptions of the lateral fornices and the rectum.[14,16,61] The use of numerical solving methods in combination with fixed instrument discretization in this work was prone to convergence issues as well as long computation times, especially in cases of small clearance, sharp curves, and discontinuities, such as stepwise input motion patterns or shapes with piecewise constant cross-section. Contact pattern-based methods may (partially) overcome these problems.[44,62] Alternatively, implicit integration schemes may improve the stability of the simulations. Moreover, to simplify the contact model one-dimensional instruments consisting of sections with constant diameter were considered, whereas the shape of the instrument may be of higher complexity. Last, channels were assumed to be rigid, whereas it may be of interest to extend these to facilitate the modeling of interstitial needle insertions in tissue.

5 | CONCLUSIONS

The multibody dynamic models developed in this article show promising results in predicting positions and forces of flexible BT instruments in curved channels of applicators. One of the benefits of these models is that these permit systematic testing of (theoretical) parameter value changes to improve our understanding of the influence of input parameters on instrument behavior. Insights obtained from these models can be used for the development of novel (patient-tailored) applicators that take into account motion and force transmission of BT instruments. This in turn may lead to more predictable instrument behavior and hence improved accuracy of treatment. Furthermore, the models may be extended to study different applicator geometries (such as split-ring applicators), flexible BT instruments (including source cables, marker wires, or sensor cables), and afterloading systems (such as forward or backward-stepping).

ACKNOWLEDGMENTS

We would like to acknowledge the contributions of Yury Niatsetski and Dr. Teunis van Manen (Elekta Brachytherapy, Veenendaal, the Netherlands) for their help with the source path simulations. The authors are grateful to Eva Hofland (Oceanz, Ede, the Netherlands) for providing the 3D-printed templates. This project was supported by a grant from the Dutch Research Council (NWO), Dutch Cancer Society (KWF), and Top Sector Life Sciences & Health (LSH) (Project No. 17921).

CONFLICT OF INTEREST STATEMENT

Remi Nout has received research grants from the Dutch Research Council (NWO), Dutch Cancer Society (KWF), Elekta, Varian, and Accuray. The remaining authors have no relevant conflicts of interest to disclose.

REFERENCES

1. Gill BS, Lin JF, Krivak TC, et al. National Cancer Data Base analysis of radiation therapy consolidation modality for cervical cancer: the impact of new technological advancements. *Int J Radiat Oncol Biol Phys*. 2014;90(5):1083-1090. doi:10.1016/j.ijrobp.2014.07.017
2. Han K, Milosevic M, Fyles A, Pintilie M, Viswanathan AN. Trends in the utilization of brachytherapy in cervical cancer in the United States. *Int J Radiat Oncol Biol Phys*. 2013;87(1):111-119. doi:10.1016/j.ijrobp.2013.05.033
3. Hellebust TP, Kirisits C, Berger D, et al. Recommendations from Gynaecological (GYN) GEC-ESTRO working group:

considerations and pitfalls in commissioning and applicator reconstruction in 3D image-based treatment planning of cervix cancer brachytherapy. *Radiother Oncol*. 2010;96(2):153-160. doi:10.1016/j.radonc.2010.06.004
4. Tanderup K, Nesvacil N, Pötter R, Kirisits C. Uncertainties in image guided adaptive cervix cancer brachytherapy: impact on planning and prescription. *Radiother Oncol*. 2013;107(1):1-5. doi:10.1016/j.radonc.2013.02.014
5. Nesvacil N, Tanderup K, Lindegaard JC, Pötter R, Kirisits C. Can reduction of uncertainties in cervix cancer brachytherapy potentially improve clinical outcome? *Radiother Oncol*. 2016;120(3):390-396. doi:10.1016/j.radonc.2016.06.008
6. Tambas M, Tavli B, Bilici N, Dizman A, Sertel H, Fayda M. Computed tomography-guided optimization of needle insertion for combined intracavitary/interstitial brachytherapy with Utrecht applicator in locally advanced cervical cancer. *Pract Radiat Oncol*. 2021;11(4):272-281. doi:10.1016/j.prro.2021.01.008
7. Dimopoulos JC, Kirisits C, Petric P, et al. The Vienna applicator for combined intracavitary and interstitial brachytherapy of cervical cancer: clinical feasibility and preliminary results. *Int J Radiat Oncol Biol Phys*. 2006;66(1):83-90. doi:10.1016/j.ijrobp.2006.04.041
8. Laan RC, Nout RA, Dankelman J, van de Berg NJ. MRI-driven design of customised 3D printed gynaecological brachytherapy applicators with curved needle channels. *3D Print Med*. 2019;5(1):1-8. doi:10.1186/s41205-019-0047-x
9. Garg A, Patil S, Siauw T, et al. An algorithm for computing customized 3D printed implants with curvature constrained channels for enhancing intracavitary brachytherapy radiation delivery. Paper presented at: IEEE International Conference on Automation Science and Engineering; 2013.
10. Patil S, Pan J, Abbeel P, Goldberg K. Planning curvature and torsion constrained ribbons in 3D with application to intracavitary brachytherapy. *IEEE Trans Autom Sci Eng*. 2015;12(4):1332-1345. doi:10.1109/TASE.2015.2475121
11. Schulman J, Duan Y, Ho J, et al. Motion planning with sequential convex optimization and convex collision checking. *Int J Rob Res*. 2014;33(9):1251-1270. doi:10.1177/0278364914528132
12. Steenhuizen J, Harbers M, Hoffmann A, De Leeuw A, Rijnders A, Unipan M. NCS Report 30: Code of Practice for Quality Assurance of Brachytherapy with Ir-192 Afterloaders. 2018:1-74. https://radiationdosimetry.org/ncs/documents/ncs-30-qa-of-brachytherapy-with-ir-192-afterloaders
13. Kohr P, Siebert FA. Quality assurance of brachytherapy afterloaders using a multi-slit phantom. *Phys Med Biol*. 2007;52(17):N387-N391. doi:10.1088/0031-9155/52/17/N03
14. Humer I, Kirisits C, Berger D, Trnková P, Pötter R, Nesvacil N. Improved source path localisation in ring applicators and the clinical impact for gynecological brachytherapy. *J Contemp Brachytherapy*. 2015;7(3):239-243. doi:10.5114/jcb.2015.52622
15. Awunor O, Berger D, Kirisits C. A multicenter study to quantify systematic variations and associated uncertainties in source positioning with commonly used HDR afterloaders and ring applicators for the treatment of cervical carcinomas. *Med Phys*. 2015;42(8):4472-4483. doi:10.1118/1.4923173
16. Goulet M, Lacroix F, Aubin S. Gynecological ring applicator: three dimensional dwell positioning accuracy, long-term stability, angular accuracy and their impact on delivered dose. *Brachytherapy*. 2016;15:S116-S117. doi:10.1016/j.brachy.2016.04.189
17. Hellebust TP, Tanderup K, Bergstrand ES, Knutsen BH, Røislien J, Olsen DR. Reconstruction of a ring applicator using CT imaging: impact of the reconstruction method and applicator orientation. *Phys Med Biol*. 2007;52(16):4893-4904. doi:10.1088/0031-9155/52/16/012
18. Nath R, Anderson LL, Meli JA, Olch AJ, Stitt JA, Williamson JF. Code of practice for brachytherapy physics: report of the AAPM radiation therapy committee task group no. 56. *Med Phys*. 1997;24(10):1557-1598. doi:10.1118/1.597966
19. Venselaar J, Pérez-Calatayud J. *A Practical Guide to Quality Control of Brachytherapy Equipment*. 1st ed. ESTRO; 2004:261.
20. Logar HBZ, Hudej R, Segedin B. Development and assessment of 3D-printed individual applicators in gynecological MRI-guided brachytherapy. *J Contemp Brachytherapy*. 2019;11(2):128-136. doi:10.5114/jcb.2019.84741
21. Kolkman-Deurloo IK, Nuyttens JJ, Hanssens PE, Levendag PC. Intraoperative HDR brachytherapy for rectal cancer using a flexible intraoperative template: standard plans versus individual planning. *Radiother Oncol*. 2004;70(1):75-79. doi:10.1016/j.radonc.2003.10.010
22. Magne N, Chargari C, SanFilippo N, Messai T, Gerbaulet A, Haie-Meder C. Technical aspects and perspectives of the vaginal mold applicator for brachytherapy of gynecologic malignancies. *Brachytherapy*. 2010;9(3):274-277. doi:10.1016/j.brachy.2009.08.014
23. Harris BD, Nilsson S, Poole CM. A feasibility study for using ABS plastic and a low-cost 3D printer for patient-specific brachytherapy mould design. *Australas Phys Eng Sci Med*. 2015;38(3):399-412. doi:10.1007/s13246-015-0356-3
24. Gulyayev V, Shlyun N. Influence of friction on buckling of a drill string in the circular channel of a bore hole. *Pet Sci*. 2016;13(4):698-711. doi:10.1007/s12182-016-0122-5
25. Huynen A. Towards a simplified stiff string model for the torque and drag problem. 34èmes Rencontres de l'AUGC. 2016:1-9.
26. Huynen A, Detournay E, Denoël V Eulerian formulation of elastic rods. *Proc Math Phys Eng Sci*. 2016;472(2190):1-23. doi:10.1098/rspa.2015.0547
27. Liu JP, Cheng ZB, Ren GX. An Arbitrary Lagrangian–Eulerian formulation of a geometrically exact Timoshenko beam running through a tube. *Acta Mech*. 2018;229(8):3161-3188. doi:10.1007/s00707-018-2161-z
28. Singh H, Hanna JA. Pseudomomentum: origins and consequences. *Zeitschrift für angewandte Mathematik und Physik*. 2020;72(3):1-25.
29. Cicconofri G, DeSimone A. A study of snake-like locomotion through the analysis of a flexible robot model. *Proc Math Phys Eng Sci*. 2015;471(2184):1-21. doi:10.1098/rspa.2015.0054
30. Dal Corso F, Misseroni D, Pugno NM, Movchan AB, Movchan NV, Bigoni D. Serpentine locomotion through elastic energy release. *J R Soc, Interface*. 2017;14(130):1-13. doi:10.1098/rsif.2017.0055
31. Ha J, Fagogenis G, Dupont PE. Modeling tube clearance and bounding the effect of friction in concentric tube robot kinematics. *IEEE Trans Rob*. 2019;35(2):353-370. doi:10.1109/TRO.2018.2878906
32. Renda F, Messer C, Boyer F. A sliding-rod variable-strain model for concentric tube robots. *IEEE Robot Autom Lett*. 2020;6(2):3451-3458. doi:10.1109/LRA.2021.3063704
33. Rucker DC, Jones BA, Webster RJ. A geometrically exact model for externally loaded concentric-tube continuum robots. *IEEE Trans Rob*. 2010;26(5):769-780. doi:10.1109/TRO.2010.2062570
34. Sharei H, Alderliesten T, van den Dobbelsteen JJ, Dankelman J. Navigation of guidewires and catheters in the body during intervention procedures: a review of computer-based models. *J Med Imaging*. 2018;5(1):1-8. doi:10.1117/1.jmi.5.1.010902
35. Lu ZH, Chen JS. Deformations of a clamped-clamped elastica inside a circular channel with clearance. *Int J Solids Struct*. 2008;45(9):2470-2492. doi:10.1016/j.ijsolstr.2007.12.004
36. Khatait JP, Krijnen M, Meijaard JP, Aarts RGKM, Brouwer DM, Herder JL. *Modelling and Simulation of a Flexible Endoscopic Surgical Instrument in a Tube*. ASME International Mechanical Engineering Congress and Exposition; 2011.
37. Hu XH, Cao L, Luo Y, Chen A, Zhang E, Zhang WJ. A novel methodology for comprehensive modeling of the kinetic behavior of steerable catheters. *IEEE/ASME Trans Mechatron*. 2019;24(4):1785-1797. doi:10.1109/TMECH.2019.2928786
38. Tang W, Lagadec P, Gould D, Wan TR, Zhai J, How T. A realistic elastic rod model for real-time simulation of

minimally invasive vascular interventions. *The Visual Computer*. 2010;26(9):1157-1165. doi:10.1007/s00371-010-0442-1
39. Tang W, Wan TR, Gould DA, How T, John NW. A stable and real-time nonlinear elastic approach to simulating guidewire and catheter insertions based on cosserat rod. *IEEE Trans Biomed Eng*. 2012;59(8):2211-2218. doi:10.1109/TBME.2012.2199319
40. Chentanez N, Alterovitz R, Ritchie D, et al. Interactive simulation of surgical needle insertion and steering. *ACM Trans Graph*. 2009;28(3):1-10. doi:10.1145/1531326.1531394
41. Takashima K, Shimomura R, Kitou T, Terada H, Yoshinaka K, Ikeuchi K. Contact and friction between catheter and blood vessel. *Tribol Int*. 2007;40(2):319-328. doi:10.1016/j.triboint.2005.10.010
42. Sharei H, Kieft J, Takashima K, Hayashida N, van den Dobbelsteen JJ, Dankelman J. A rigid multibody model to study the translational motion of guidewires based on their mechanical properties. *J Comput Nonlinear Dyn*. 2019;14(10):1-7. doi:10.1115/1.4043618
43. Bentley M, Rucker C, Reddy C, Salzman O, Kuntz A. Safer motion planning of steerable needles via a shaft-to-tissue force model. *arXiv*. 2022;2022:1-17. arXiv:2101.02246
44. Liu J, Cao L, Miyasaka M, Phee SJ. A frictional contact-pattern-based model for inserting a flexible shaft into curved channels. *IEEE/ASME Trans Mechatron*. 2021;27(5):1-12. doi:10.1109/tmech.2021.3111701
45. Jonker JB, Meijaard JP. SPACAR - computer program for dynamic analysis of flexible spatial mechanisms and manipulators. In: Schiehlen W, ed. *Multibody Systems Handbook*. 1st ed. Springer-Verlag Berlin Heidelberg; 1990:123-144.
46. Khatait JP, Brouwer DM, Meijaard JP, Aarts RGKM, Herder JL. Flexible multibody modeling of a surgical instrument inside an endoscope. *J Comput Nonlinear Dyn*. 2014;9(1):1-11. doi:10.1115/1.4026059
47. Jonker B. *A Finite Element Dynamic Analysis of Flexible Spatial Mechanisms and Manipulators*. Doctoral Dissertation. Delft University of Technology; 1988.
48. Alderliesten T, Konings MK, Niessen WJ. Simulation of minimally invasive vascular interventions for training purposes. *Comput Aided Surg*. 2004;9(1):3-15. doi:10.3109/10929080400006408
49. D'Errico J. distance2curve. MATLAB Central File Exchange. Accessed Dec 13, 2022, https://nl.mathworks.com/matlabcentral/fileexchange/34869-distance2curve
50. Schwab AL, Meijaard JP. How to draw Euler angles and utilize Euler parameters. Paper presented at: ASME 2006 International Design Engineering Technical Conferences & Computers and Information in Engineering Conference; 2006; Philadelphia, PA, USA.
51. Armstrong B, Canudas de Wit C. Friction modeling and compensation. In: Levine WS, ed. *The Control Handbook*. CRC Press; 1996:1369-1382.
52. Shampine LF, Gordon MK. *Computer Solution of Ordinary Differential Equations: The Initial Value Problem*. W.H. Freeman and Company; 1975.
53. Zhuang Y. *Real-Time Simulation of Physically Realistic Global Deformations*. Doctoral Dissertation. University of California; 2000.
54. Straathof R, Meijaard JP, van Vliet-Pérez S, et al. Code underlying the publication: Multibody dynamic modeling of the behavior of flexible instruments used in cervical cancer brachytherapy. 4TUResearchData. doi:10.4121/21714143
55. Berger D, Dimopoulos J, Georg P, Georg D, Potter R, Kirisits C. Uncertainties in assessment of the vaginal dose for intracavitary brachytherapy of cervical cancer using a tandem-ring applicator. *Int J Radiat Oncol Biol Phys*. 2007;67(5):1451-1459. doi:10.1016/j.ijrobp.2006.11.021
56. Elekta. Oncentra® Brachy v4.6 - Physics and Algorithms. 2018:1-188.
57. Lang H, Linn J, Arnold M. Multibody dynamics simulation of geometrically exact cosserat rods. *Multibody SysDyn*. 2013;25(3):285-312.
58. Niatsetski Y, Fekkes S, Vreeken H. Source path measurements for ring applicators. *Radiother Oncol*. 2011;99(1):S278. doi:10.1016/s0167-8140(11)70817-9
59. Palmer A, Mzenda B. Performance assessment of the BEBIG MultiSource high dose rate brachytherapy treatment unit. *Phys Med Biol*. 2009;54(3):7417-7434. doi:10.1088/0031-9155/54/24/011
60. Fonseca GP, Van Den Bosch MR, Voncken R, Podesta M, Verhaegen F. A novel system for commissioning brachytherapy applicators: example of a ring applicator. *Phys Med Biol*. 2017;62(21):8360-8375. doi:10.1088/1361-6560/aa8d0a
61. Awunor OA, Dixon B, Walker C. Direct reconstruction and associated uncertainties of 192Ir source dwell positions in ring applicators using gafchromic film in the treatment planning of HDR brachytherapy cervix patients. *Phys Med Biol*. 2013;58(10):3207-3225. doi:10.1088/0031-9155/58/10/3207
62. Denoël V, Detournay E. Eulerian formulation of constrained elastica. *Int J Solids Struct*. 2011;48(3-4):625-636. doi:10.1016/j.ijsolstr.2010.10.027
63. Jonker JB, Meijaard JP. Deformation modes and dual stress resultants of spatial beam elements in large deflection multibody system analyses. Paper presented at: The 2nd Joint International Conference on Multibody System Dynamics; 2012; Stuttgart, Germany.

SUPPORTING INFORMATION

Additional supporting information can be found online in the Supporting Information section at the end of this article.

How to cite this article: Straathof R, Meijaard JP, van Vliet-Pérez SM, et al. Multibody dynamic modeling of the behavior of flexible instruments used in cervical cancer brachytherapy. *Med Phys*. 2024;1-13. https://doi.org/10.1002/mp.16934